JOINT EUROPEAN TORUS

JET–P(90)18

K-D Zastrow, H.W. Morsi, M. Danielsson, M.G von Hellermann, E. Kallne,
R. Konig, W. Mandl, H.P. Summers and JET Team

Deduction of Central Plasma Parameters from Line-of-Sight Averaged Spectroscopic Observations

“This document contains JET information in a form not yet suitable for publication. The report has been prepared primarily for discussion and information within the JET Project and the Associations. It must not be quoted in publications or in Abstract Journals. External distribution requires approval from the Publications Officer, JET Joint Undertaking, Abingdon, Oxon, OX14 3EA, UK”.

“Enquiries about Copyright and reproduction should be addressed to the Publications Officer, EFDA, Culham Science Centre, Abingdon, Oxon, OX14 3DB, UK.”

The contents of this preprint and all other JET EFDA Preprints and Conference Papers are available to view online free at www.iop.org/Jet. This site has full search facilities and e-mail alert options. The diagrams contained within the PDFs on this site are hyperlinked from the year 1996 onwards.

Deduction of Central Plasma Parameters from Line-of-Sight Averaged Spectroscopic Observations

K-D Zastrow[1], H.W. Morsi, M. Danielsson[1], M.G von Hellermann,
E. Kallne[1], R. Konig, W. Mandl, H.P. Summers and JET Team*

JET-Joint Undertaking, Culham Science Centre, OX14 3DB, Abingdon, UK

[1]Department of Physics I, Royal Institute of Technology, 10044 Stockholm, Sweden
** See Appendix 1*

Preprint of Paper to be submitted for publication in
Physics Review A

Deduction of central plasma parameters from line-of-sight averaged spectroscopic observations

K.-D. Zastrow ♣, *H.W. Morsi, M. Danielsson* ♣,
M.G. von Hellermann, E. Källne ♣, *R. König, W.Mandl, H.P. Summers*

JET Joint Undertaking, Abingdon,
OX14 3EA, Great-Britain
♣Department of Physics I, Royal Institute of Technology
10044 Stockholm, Sweden

Abstract

A method is presented to deduce central ion temperature and toroidal rotation velocity from line-of-sight averaged x-ray spectra from hot plasmas. The analysis is based on atomic data for the processes that give rise to x-ray spectral lines. Combined with measured electron temperature and density profiles a synthetic spectrum is calculated. The fit of this synthetic spectrum to the observed one gives a new level of accuracy to line-of-sight integrated observations in a considerably extended range of ion temperatures and toroidal rotation velocities. The choice of model for radial profiles for ion temperature and toroidal rotation velocity is shown not to be critical.

The concentration of the emitting impurity is deduced from the total line intensity, making use of the absolute calibration of the detector sensitivity. As a new result, the average plasma charge Z_{eff} is derived from the absolute level of the continuum radiation. These measurements are based on atomic data for x-ray line and continuum radiation and measured electron temperature and density profiles.

The results for ion temperature and toroidal rotation velocity are compared with those from visible charge exchange spectroscopy. The observed visible lines are shifted in wavelength, and their width is reduced, due to the velocity dependence of the cross section for the charge transfer from the neutral beam particles to the observed impurities. The theoretically predicted magnitude of these effects is verified. When the results from visible charge exchange spectroscopy are corrected for the cross section effects, excellent agreement between both methods is obtained.

I. Introduction

X-ray spectroscopy is a powerful tool for diagnosing the properties of hot plasmas. Through observations of high resolution x-ray spectra from highly charged metal impurities it has been possible to deduce crucial plasma parameters such as ion temperature and toroidal rotation from spectral line shapes and shifts[1]. However, it has not been possible to account for, with sufficient accuracy, that the emitting ions are embedded in a plasma with spatial distributions of parameters such as temperatures and densities. To take this into account, the radial distribution functions must be measured or modelled and the atomic data describing ionisation, recombination and excitation of the ions must be known over a wide range of parameters. This is especially important, when the width of the plasma region that emits the observed spectrum becomes large compared with the scale length on which the quantities that are to be measured change.

In this paper, we will present and test a technique, which extends the application of line-of-sight observations towards the deduction of central plasma parameters by giving special attention to radial distributions. With this technique, the accuracy of the results is significantly increased over an extended range of plasma parameters, such as ion and electron temperatures and toroidal rotation velocities.

The method is based upon atomic data for the processes that give rise to both line and continuum emission in the plasma[2,3,4]. With these data, the radial distribution of the absolute level of the x-ray emission is calculated from measured electron temperature and density profiles. The spectral distribution is described by a model for radial ion temperature and toroidal rotation velocity profiles to obtain the shape and shift of the observed spectral lines, respectively, after integration along the line-of-sight.

The central ion temperature, central toroidal rotation velocity and nickel concentration are the results of a fit of the complete calculated spectrum, including satellite lines, to the observed one. The effective plasma charge Z_{eff} is obtained by a fit of the calculated x-ray continuum to the observed background. Both measurement of nickel concentration and Z_{eff} rely upon the absolute calibration of the x-ray detector sensitivity.

In addition to the main objective, namely including line-of-sight averaging in the analysis, this method consistently describes all effects that modify the related observed quantities. Collective plasma velocities in JET are comparable to the ion thermal velocities. The shear in the toroidal rotation profile therefore gives rise to an additional line broadening, which is thus considered. Since the unresolved dielectronic satellite lines are included in the calculation, their contribution to the line broadening and apparent shift is taken care off. The slight slope in the continuum is reproduced, since it stems from the variation of the observed plasma column length with Bragg angle.

In the first section of this paper, we will describe the model calculations. We will then discuss the accuracy of the input data and model assumptions and their influence on the results. In the last section, we will present a comparison of the results for ion temperature and toroidal rotation with those from visible charge exchange spectroscopy (CXRS)[5]. Due to the velocity dependence of the cross section for the charge transfer from the neutral beam particles to the observed impurities, the observed visible lines are shifted in wavelength, and their width is reduced. It has here been possible to verify the theoretically predicted magnitude of these effects[6] by means of a comparison over a wide range of ion temperatures. Finally, the comparison is extended towards CXRS results, that have been corrected for these cross section effects.

II. The high resolution x-ray crystal spectrometer

The x-ray crystal spectrometer currently observes the resonance line w of helium-like nickel (1s2p $^1P_1 \rightarrow$ 1s^2 $^1S_0$) at 1.5856 Å(7.82 keV). This line is chosen, since nickel is the most prominent metal impurity in JET, with concentrations in the range of $2{\cdot}10^{-7}$ to 10^{-3} of the electron density, and the effective emissivity of w is the largest from all nickel ionisation stages for the typical JET electron temperatures up to 11 keV. Here we will only describe the features of the instrument, that are of interest for this work. More details can be found elsewhere[7,8].

The instrument is a bent x-ray crystal spectrometer, with a diameter of the Rowland circle of approximately 20 m (See Figure 1). The spectrometer line-of-sight has a distance of closest approach to the torus axis of 1.82 m. This geometry allows an observation of the toroidal component of the plasma rotation. The data in this paper have been acquired using a germanium crystal. With this crystal, the spectrum

of helium-like nickel is observed in second order diffraction with a resolution $\frac{\lambda}{\Delta\lambda}$ of 20000, due to the 1.27 mm separation of the wires in the multiwire ionisation chamber. The ionisation chamber is operated outside its proportional range and is thus also sensitive to first and third order diffraction of the crystal, i.e. to radiation at 3.17 Å(3.91 keV) and 1.06 Å(11.73 keV). Higher diffraction orders are negligible. In table I we give results for the luminosity L of the crystal, the relative detector efficiency η, the transmission of the rest of the diagnostic system T and the resulting absolute calibration factors $S = LT\eta$ for a detector chamber voltage of 4300 V for all three photon energies. The calibration of the wavelength scale of the spectrometer is discussed in III.2.2.

III. Analysis of spectra

III.1. Description of the model fit

The atomic data for the nickel ionisation balance and for the line formation mechanisms of helium-like nickel have been tested for the conditions at JET[2,3]. The model is capable to describe the line ratios of satellite lines to the resonance line very well. Especially, the structure of the resonance line with its close-lying dielectronic satellites can be reproduced as a function of electron temperature. This is important for an analysis of the ion temperature and toroidal rotation, since the satellite lines give rise to both an additional line broadening and an apparent shift of the resonance line. These effects are thus considered.

The intensity of each spectral line as a function of radius R can be expressed as

$$I(R) = n_e(R) \cdot n_{Ni}(R) \cdot \epsilon_{eff}(T_e(R))$$

where n_e and n_{Ni} are the number densities of electrons and nickel and ϵ_{eff} is the effective emissivity of the spectral line. In figure 2, ϵ_{eff} is shown for the resonance line w of helium-like nickel. The contribution from the different line formation mechanisms as well as the fractional abundances of nickel ionisation stages are already included. For all lines, ϵ_{eff} is a function of T_e alone. This is due to the high ionic charge (+26) and low electron density ($\leq 1 \cdot 10^{15} cm^{-3}$).

At each radial position, the spectral intensity $I(R, \lambda)$ is obtained using a Voigt function for the resonance line and Gaussians for all other lines.

The Voigt function is a convolution of a Gauss and a Lorentz function, which accounts for the Doppler broadening and the natural line shape, respectively. The latter is important for the resonance line only, since its radiative transition probability is much higher than for all other lines. Its natural line width (FWHM) is $\Delta\lambda = 8.21 \cdot 10^{-15}$ m.

The spectra are displaced in wavelength according to the projection of the toroidal velocity on the line-of-sight, and then integrated over all radii. The observed spectral range covers the resonance line w, the close lying unresolved dielectronic satellite lines as well as the resolved transitions x (1s2p $^3P_2 \rightarrow$ 1s^2 $^1S_0$) and t (1s2p (^3P) 2s $^2P_{\frac{1}{2}} \rightarrow$ 1s^2 2s $^2S_{\frac{1}{2}}$) in helium-like and in lithium-like nickel, respectively. Typically, 160 channels are available for the fit, of which approximately 20 on the short wavelength side are free of spectral lines. The ion temperature $T_i(0)$ and the toroidal rotation frequency $\omega_{rot}(0)$ at the magnetic axis as well as the fraction of nickel $f_{Ni} = n_{Ni}/n_e$ are determined by performing a least-squares fit of the synthetic spectrum to the observed one with respect to these parameters. The central values are based on a model for $T_i(R)$ and $\omega_{rot}(R)$, which will be discussed in section III.4.

The continuum level is modelled integrating bremsstrahlung and recombination radiation from the bulk plasma (H, He), light impurities (Be, C and O) and nickel along the line-of-sight, using the effective continuum emissivities at the three discrete energies 3.91 keV, 7.82 keV and 11.73 keV[4]. Considering the calibration factors (see Table I), typically 50 to 80 % of the observed background stems from continuum emission at 3.91 keV, 20 to 50 % at 7.82 keV and less than 10% at 11.73 keV. The slight slope in the continuum stems from the variation of the observed plasma column length as function of Bragg angle.

The nickel concentration is given from the absolute intensity of the helium-like nickel lines, and thus the contribution of nickel to the continuum (typically 5 % at a nickel concentration of 0.01 %) is known. For a given bulk plasma composition H : He and light impurity composition Be : C : O, the ratio of light impurities to bulk plasma density is adjusted in the model, to obtain the observed background. From these results, Z_{eff} can be calculated.

In addition to $T_i(0)$, $\omega_{rot}(0)$, f_{Ni} and the fraction of light impurities, two more quantities are fitted. These are correction factors for the intensities of the satellite lines x and t. In the case of x, it has been shown, that the atomic physics data are erroneous[3] which is the reason for the introduction of this parameter. The correction factor for t is introduced as a monitor for the electron temperature input data (See III.3).

Note also, that the wavelength of x is reduced in our analysis by 0.204 mÅ from 1.5897 Å to 1.5895 Å, corresponding to 2.66 channels, which has been determined from model fits with this shift as an additional free parameter. Analysing 1300 spectra in this way, the value has been determined with a standard deviation of 0.021 mÅ. The wavelength of the resonance line for comparison is 1.5856 Å [2]. Similarly, the wavelength of t (1.5911 Å) has been determined to be correct.

A typical result for the analysis is shown in Fig. 3. The input data for electron temperature and density are shown in Fig. 4. In this case, we assumed that the ion temperature profile is characterised by a peaking parameter γ_T and the profile for the toroidal rotation velocity by a peaking parameter γ_ω as measured by visible charge exchange recombination spectroscopy (CXRS). (See III.4 for a definition of peaking parameters). The corresponding central values are determined from the fit. In Figs. 5 and 6 we show the result of the fit in comparison with the measured radial profiles from CXRS. The apparent ion temperature and the line-of-sight average toroidal rotation velocity, not applying the procedure described above, are also shown. As can be seen, the difference between apparent and central value is large in this case, which is also suggested from the CXRS data.

In the following sections, we will carry out the error analysis for the measurements of the central ion temperature, the central toroidal rotation frequency, the nickel concentration and the effective plasma charge. The numerical results for this analysis are summarised in table II.

III.2. Intrinsic uncertainties

There are two sources of error from the least-squares fit analysis of the spectrum. One is count rate statistics, which will have impact on all results. The other is the uncertainty in the absolute calibration of the wavelength scale, which will influence the results for the toroidal rotation velocity only. For the measurement of the absolute level of radiation, and hence for the nickel concentration and effective plasma charge, the accuracy of the absolute calibration of the sensitivity of the instrument is important.

III.2.1. Errors due to count rate statistics

In order to quantify the effect of count rate statistics, the following procedure has been applied. Starting with a given case, 500 spectra were simulated from the original fit, applying a random variation to the expectation value for the counts in each channel with Poisson characteristic. These 500 spectra were then analysed with the same electron and model profiles as the original. The results for the central ion temperature, toroidal rotation and nickel concentration then have a standard deviation, which is a measure for the uncertainty. The average values display no significant change, showing that there is no systematic error due to count rate statistics.

The statistical errors that are actually applicable for our measurements will depend on the nickel concentration. It is not useful to aim at high intensity, i.e. good statistics, if the nickel concentration is low, since this means uncertainty due to time averaging. Thus, the values in table II represent upper limits.

III.2.2. Wavelength calibration

The calibration of the wavelength scale is based on the assumption, that the plasma is not rotating during the ohmic phase of JET discharges, i.e., in the absence of additional heating. The model fit is performed with respect to the channel number that corresponds to the wavelength of the resonance line. Thus, the shift of the apparent peak position by dielectronic satellites, which depends on the electron temperature and density and on the ion temperature, is taken into account. Statistics for the observed position during several discharges is then made.

The distribution of peak positions on which the calibration is based has a standard deviation from the average channel which is only slightly larger than expected from count rate statistics. This indicates, that the plasma is indeed not rotating strongly during the ohmic phase. It is mainly count rate statistics that determines the uncertainty of the wavelength scale calibration.

In the dataset used here, 826 observations from a range of 110 consecutive JET-discharges are included, for which the integration time of the spectrum is less or equal to 0.08 secs. Thus, the electron temperature and density profiles should be representative for the whole spectrum integration time. When restricting the data set to even shorter integration

times the average value stays constant. When we do not subtract the dielectronic satellites, the average peak position is 0.62 ± 0.3 channels higher, corresponding to an apparent rotation frequency of 5.0 krad/s. The mean value and, especially, the width of this distribution of position differences should, however, be regarded as representative for the influence of electron temperatures and densities on the line position in this specific dataset.

III.3. Discussion of input data

In order to simulate the spectrum, measured profiles for electron temperature and density are needed. In this section, we analyse the influence of uncertainties in these input data on the results of our measurements.

III.3.1. Electron temperature data

There are two possible sources for the electron temperature profiles at JET, namely electron cyclotron emission (ECE)[9] and Thomson scattering (Light detection and ranging, LIDAR)[10]. In addition, there are two more possible sources for the line average electron temperature, namely pulse height analysis (PHA)[11] and, from our x-ray spectra, line intensity ratios from helium-like nickel. It has been shown, that the line ratios agree better with the electron temperatures from LIDAR and PHA[3]. Therefore, the results of the method described here are expected to be more accurate, when the calculated emissivity profiles are based on LIDAR electron temperature data. However, the ECE data have the better time resolution of the two profile measurements. Thus, we will mostly use ECE profiles. In order to monitor the effects of electron temperature data on our spectra, a correction factor for the observed intensity of the satellite line t is introduced.

The observed difference between ECE and LIDAR is, that the ECE typically gives 10% higher electron temperatures[12]. Performing the analysis of the spectra with ECE data instead of LIDAR data, the results change typically according to table II. The changes are due to the behaviour of ϵ_{eff} in figure 2. Higher electron temperature input data result in an increased calculated emission from parts of the plasma with lower ion temperature. Thus, the apparent ion temperature has to be reproduced by an increase of the ion temperature on axis.

In the case of the results for the toroidal rotation, a similar effect is partly compensated for by the apparent shift of the line due to dielectronic satellites. Their intensity, and thus their calculated influence, decreases with increasing electron temperature. In the case of rotation away from the spectrometer, these effects would add.

Figure 2 shows, that the maximum of the emissivity of w is at 8 keV. This reduces the sensitivity to errors in the electron temperature input data for the nickel concentration results, when $T_e(0) \geq 8$ keV. The calculated decrease of the intensity in the plasma center is compensated by an increase further outside, giving a similar overall intensity. The results for Z_{eff} are less sensitive to the electron temperature profile data than the nickel concentration.

The other possible error in the electron temperature is of statistical nature. In order to estimate the effect of this on the results of the model fit, spectra have been analysed with input data, where in every radial position the values have been randomly varied with Gaussian characteristic. Repeating this 500 times, the results for ion temperature, toroidal rotation and nickel concentration vary as well. The results for an error of 5%, which is typical for LIDAR data, are summarised in table II. The statistical error for the ECE data is negligible. Note, that a statistical error in the electron temperature results in both statistical and systematic errors of the measured quantities due to the non-linear nature of ϵ_{eff}.

III.3.2. Electron density data

There are two possible sources for electron density profiles at JET, LIDAR and interferometry. Again, we will normally use interferometry data, because of the better time resolution. However, if we use LIDAR temperatures, we will also use LIDAR densities, since they are measured for the same radial positions.

At JET, interferometry and LIDAR measurements of electron density profiles are coordinated[12]. This means that the absolute level of the LIDAR results is calibrated against the interferometry data to give the same line integrated density. Since the emissivities are not a function of electron density, uncertainties of the absolute level of n_e will not influence the results for $T_i(0)$ and $\omega_{rot}(0)$. Using the assumption, that $n_{Ni}(R) = f_{Ni} \cdot n_e(R)$ (see III.4), the error of the nickel concentration is twice as large as the error of the electron density. The same result is obtained for the effective plasma charge.

The influence of the profile shape on our measurements of ion temperature and toroidal rotation is minute. The results for f_{Ni} and Z_{eff}, however, are strongly influenced, as can be seen in table II.

With a statistical error in every radial position of 10%, typical for LIDAR data, using the same procedure as described for the electron temperature, the resultant errors of the measurements are summarised in table II. Interferometry data do not have statistical errors of this nature, since the profile is obtained by Abel inversion. Statistical errors thus affect the profile shape, which has already been discussed above.

III.4. Discussion of model assumptions

The central values for ion temperature, toroidal rotation and nickel concentration which we obtain from our model fit are based on assumptions for the profile shapes of these quantities. The implications of these asumptions on the results are discussed in the following.

Note, that the results for Z_{eff} are not influenced by these assumptions. Likewise, the results for the nickel concentration are independent of the model for the ion temperature and the toroidal rotation frequency profiles.

III.4.1. Nickel concentration profile

In this work, the assumption is, that the nickel concentration is constant over the whole plasma. Assuming a different profile has only minute effects on $T_i(0)$ and $\omega_{rot}(0)$, which means, that the assumption is not critical. More specifically, it is not necessary to include particle transport in our model, which simplifies the procedure significantly.

III.4.2. Ion temperature profile

We will use two different approaches. We will either assume

$$T_i(R) = T_i(0) \cdot \frac{T_e(R)}{T_e(0)}$$

i.e. that the ion temperature profile is proportional to the electron temperature profile, or that

$$T_i(R) = T_i(0) \cdot \exp(-\gamma_T \cdot \Psi(R)^{\frac{3}{4}})$$

Here, $\Psi(R)$ is the flux surface label from magnetic equilibrium calculations, and γ_T is the peaking parameter. This functional form is chosen, since the CXRS profiles are usually fitted well by this expression in the central part of the plasma[5]. The peaking parameter may either be chosen constant or taken from CXRS. The latter approach will then imply the assumption, that

$$T_i(R) = T_i(0) \cdot \frac{T_{i,CXRS}(R)}{T_{i,CXRS}(0)}$$

The measured range of peaking parameters γ_T is 0.35 to 3.25. About 75% of all cases lie in the interval from 1.0 to 2.1, with an average of 1.5. A correlation of γ_T with neutral beam power per particle $\frac{P_{NBI}}{n_e}$ is observed. For low beam power per particle, the ion temperature profile resembles the electron temperature profile, which makes both model assumptions practically converge.

In Fig. 7 we illustrate the effect of the choice of model function for $T_i(R)$ on the determined central ion temperature for the example shown in figure 3. The peaking parameter from CXRS is close to the average peaking parameter. Within an interval for γ_T from 1.0 to 2.1, the resultant ion temperature changes by less than 10%. In other words, analysing spectra with the average peaking parameter of 1.5 will yield ion temperatures with an accuracy better than 10% for about 75% of all cases during NBI. In this case, the result based on the assumption that the ion temperature profile resembles the electron temperature profile differs by more than 10%. This shows, that during high power NBI this assumption is not valid. However, it should still be reasonable for other plasma heating scenarios, or when the NBI power is low.

Whilst the choice of model function for $T_i(R)$ has a strong influence on the determined central ion temperature, it has only a marginal effect on $\omega_{rot}(0)$. This shows, that the toroidal rotation velocity can be measured without any knowledge of the ion temperature profile.

III.4.3. Toroidal rotation velocity profile

In this work, we use a model function similar to that for the ion temperature profile, namely

$$\omega_{rot}(R) = \omega_{rot}(0) \cdot \exp(-\gamma_\omega \cdot \Psi(R)^{\frac{3}{4}})$$

Again, γ_ω may be assumed constant or be taken from CXRS data. The observed values from CXRS range from 0.5 to 2.5 with about 80% of all cases in the range of 1.0 to 2.1. Again, a correlation of γ_ω with neutral beam power per particle is observed.

Note, that when we use the peaking parameter from CXRS, we will actually assume

$$\omega_{rot}(R) = \Delta\omega + \omega_{rot,CXRS}(0) \cdot \exp(-\gamma_\omega \cdot \Psi(R)^{\frac{3}{4}})$$

since we expect the difference $\Delta\omega$ between the two measurements to stem from uncertainties in the calibration of the absolute wavelength scale (See III.2).

Like in the case of the ion temperature profile, the choice of $\omega_{rot}(R)$ affects mainly the result for the related central value. In Fig. 8 we show the results for $\omega_{rot}(0)$ and $T_i(0)$ as a function of γ_ω for the example in figure 3. Also indicated is the value obtained using γ_ω from CXRS, which falls well within the trend of the other points, despite the different model functions used. Within an interval for γ_ω from 1.0 to 2.2, the result for the central toroidal rotation changes by less than 10% and the result for the central ion temperature by less than 6%. The effect on the ion temperature measurement is due to the change of the velocity shear. A decrease of γ_ω results in an increase of $T_i(0)$.

Note, that the choice of model function causes a relative change in the toroidal rotation. All the error sources discussed so far cause absolute uncertainties.

III.5. Summary of error analysis

We can now summarise the uncertainties introduced by the intrinsic errors due to count rate statistics, absolute sensitivity and wavelength

calibration, by the errors in the input data and by the model assumptions.

For the central ion temperature, the effects due to count rate statistics and the uncertainties in $T_e(R)$ at high electron temperatures dominate. All other effects from the input data are much smaller. When model fits are performed as a consistency check with CXRS data, the peaking parameters γ_T and γ_ω are known within $\pm$ 0.1. The overall uncertainty of $T_i(0)$ is then expected to be better than 15%.

For the toroidal rotation, the wavelength calibration and count rate statistics are dominating the error, when peaking parameters γ_ω from CXRS are used to perform a consistency check. The overall uncertainty thus becomes $\pm$ 5.0 krad/s.

As shown above, the influence of model assumptions becomes larger in the absence of measured profile functions. For the ion temperature, the expected error then increases to about 20%. For the toroidal rotation a significant increase of the uncertainty may be expected when $\omega_{rot} \geq$ 50.0 krad/s. The latter implies, that, in the absence of NBI, the choice of model function is not critical for the measurement of ω_{rot}.

For the nickel concentration and the effective plasma charge, the dominating sources of error are introduced by the input data for electron temperature and density. Together with the uncertainty of the absolute level of intensity from the calibration, 25% error is expected for the nickel concentration. For the effective plasma charge the error is about 30%.

IV. Comparison with other diagnostic techniques

In addition to x-ray cystal spectroscopy, three passive and one active diagnostic techniques are currently used, to measure the ion temperature on the JET tokamak: total neutron yield emission[13], Doppler line width from neutron time of flight measurements[14], velocity distribution of neutral particles[15] and CXRS[5,6].

Each of these four techniques has its own limitations. The neutron yield requires the knowledge of the central deuteron density and relies on a fusion rate coefficient for thermal ions. Thus, this method cannot be used during additional heating, such as ion cyclotron resonance heating (ICRH) and neutral beam injection (NBI), where the fusion rate

is dominated by non-thermal particles. Neutron spectroscopy normally does not allow a time resolution comparable to the other diagnostics, since the number of observed neutrons is not sufficient to achieve good statistics. The analysis of neutral particle energy spectra has to be corrected for multiple step processes for particles escaping the hot core. In addition to this the high noise level, caused by enhanced neutron fluxes, prevents any operation during NBI. However, the particle fluxes are high and allow good temporal resolution.

CXRS allows measurements of radial ion temperature and toroidal rotation velocity profiles with a spatial resolution of better than 2% of the major radius and ion temperature errors $\leq 10\%$. It requires, however, a sufficiently high neutral beam power and energy to overcome signal-to-noise problems at high electron densities $\geq 1.0 \cdot 10^{14} cm^{-3}$, where typical temperature errors are up to 30%. Since radial profiles are available from this diagnostic, we chose to test our analysis method by comparing the results for ion temperature and toroidal rotation with the results from CXRS.

The example presented in Fig.3 shows, that the difference between apparent and central values for ion temperature and toroidal rotation obtained by the model fit may be large. However, a large number of cases exists, where the differences are negligible, especially during ohmic phases of JET discharges with central electron temperatures well below 8 keV and weak toroidal rotation. In this chapter we are mainly interested in cases that yield large differences.

In Fig. 9 the apparent and central values for the ion temperature are compared with the results from CXRS. Time slices from various discharges were selected under the condition, that beam penetration in the plasma center was better than 20% to guarantee reliable CXRS results. We used the analytical model with peaking parameters γ_T from CXRS for this consistency check. Similarly, in Fig.10 line average and central values for the rotation frequency are compared. Again, peaking parameters γ_ω for the model fit are taken from CXRS.

As can be seen, the model fit results show good agreement with CXRS values over a much wider range of ion temperature and rotation frequencies. The scatter is reduced significantly. However, both ion temperature and toroidal rotation from CXRS are on average lower than the model fit results. This will be discussed in the following.

IV.1. Cross section dependence of CXRS results

The CXRS spectra are the result of charge transfer from deuterium in the heating beam to bare nuclei of carbon in the plasma. The effective emission cross section depends on the collision energy of the deuterium atoms in the frame of reference of the carbon nuclei. At JET, the beam particles have energies of 40 keV/amu, 40/2 keV/amu and 40/3 keV/amu. This has to be compared with the emission cross section for the charge exchange spectral line, which has its maximum at 45 keV/amu.

The observed spectrum can be simulated by integrating the cross section over a thermal population of carbon nuclei with a given ion temperature and velocity relative to the beam for the three beam components. The emitted spectrum shows a red shift and a reduced line width, as a result of the slope and curvature of the cross section, respectively[6]. The reduction of the central rotation frequency calculated from the red shift increases from about 5 krad/s at an ion temperature of 4 keV to 20 krad/s at 30 keV. This corresponds to the difference observed in Fig. 10. The corresponding correction for the central ion temperature is only marginal, i.e. less than 5 %. In addition, the observed profile functions, reflected by the peaking parameter, change when the corrections are applied. Typically, γ_ω increases by 0.1, whilst γ_T increases by 0.02.

IV.2. Comparison with corrected CXRS results

In order to study further the comparison between the two techniques, CXRS results have been corrected for the cross section effects presented above. In Figs. 11 to 13 we present this comparison as function of time during the NBI phase of a JET plasma discharge.

In Fig. 11, the apparent ion temperature from XCS is shown, compared with two different results from the model fit. As a consistency check, we assumed analytical ion temperature profiles in one case, using γ_T from CXRS and in the other case we assumed, that the ion temperature profile is proportional to the electron temperature profile. As can be seen, the latter gives lower results, since electron temperatures are less peaked. However, sawteeth are less pronounced for the analytic model. This is due to the input peaking parameters from CXRS. The CXRS does not resolve the changes in the ion temperature profile on the time scale of the XCS measurements. The time resolution of the CXRS system is 100

msec, with a spectrum taken during 50 msec and 50 msec interval to clear the signal. The time resolution for the XCS for comparison is 20 msec. Furthermore, the CXRS detector does not clear the signal completely, which results in additional time averaging.

In Fig. 12, we show the comparison of the model fit results, using the assumption that the ion temperature profile is proportional to the electron temperature profile, with two CXRS signals, namely central chord and horizontal line-of-sight. In the beginning of the NBI phase, the model fit results agree well with the data from the central chord spectrometer, which has a time resolution and response comparable to the XCS. During the NBI phase, the location of the magnetic axis moves and the vertical chord does not observe the plasma centre anymore.

In Fig. 13 the central rotation frequency is shown, comparing apparent XCS, central XCS from the model fit and central CXRS values. For the model fit, peaking parameters γ_ω from CXRS have been used. The agreement between the signals requires that the CXRS results be corrected for cross section effects. Before the correction applied here, the values are 5 to 15 krad/s lower than shown. In the correction, it has been assumed that the plasma is at rest. A further small correction of CXRS data towards higher values could be expected if the correct velocity was used. This could account for the remaining differences between the two measurements.

The importance of the model fit is most pronounced in the behaviour between 50.0 secs and 50.3 secs, where the line average rotation frequency from XCS stays high, but the model fit result falls to the level from CXRS. This is due to a collapse of the rotation profile.

V. Conclusions

We have shown, that passive line-of-sight averaged spectroscopic measurements of central plasma parameters can successfully be based upon model calculations of the emission profiles. This requires reliable input data for electron temperature and density, which are available in most laboratory plasma experiments. The model assumptions influence the results. However, the improvement over a wide range of plasma conditions compared to the observation of line-of-sight average line width and position is significant.

Furthermore, we have shown, that the emission process of charge exchange spectra gives rise to an apparent shift and reduced line width

of the predicted magnitude, which have to be taken into account in a comparison with the XCS results. This is particularly important for the rotation velocity measurements.

When both improved analysis methods are applied, the two techniques show excellent agreement.

Acknowledgments

We would like to thank B.Viaccoz and J.Holm for technical services and R. Barnsley for expertise and participation in improving the detector and crystal performance. We are indebted to E. Oord and J.Ellis for constant programming support, E. Springmann for help with the use of his magnetic flux surface code and D. Pasini for assistance in the compilation of the bremsstrahlung data.

References

1) F. Bombarda, R. Giannella, E. Källne and G.J. Tallents, J.Quant.Spectrosc.Radiat.Transfer. **41**,323(1989)

2) F. Bombarda, R. Giannella, E. Källne, G.J. Tallents, F. Bely-Dubau,P. Faucher, M. Cornille, J. Dubau and A.H. Gabriel, Phys.Rev. **A37**,504(1988)

3) K.-D. Zastrow, E. Källne and H.P. Summers, Phys.Rev. **A41**,1427(1990)

4) A. Weller, D. Pasini, A.W. Edwards, R.D. Gill and R. Granetz, JET-IR(87)10

5) H. Weisen, M.G. von Hellermann, A. Boileau, L.D. Horton, W. Mandl and H.P. Summers, Nucl. Fusion **29**,2187(1989)

6) M.G. von Hellermann, W. Mandl, H.P. Summers, H. Weisen, A. Boileau, P.D. Morgan, H.W. Morsi, R. König, M.F. Stamp and R. Wolf, Rev.Sci.Instr. **61**,(1990) (in press)

7) R. Bartiromo, F. Bombarda, R. Giannella, L. Panaccione and G. Pizzicaroli, Rev.Sci.Instr. **60**,237(1989)

8) H.W. Morsi, R. Barnsley and R. Giannella, to be prepared

9) D.V. Bartlett, E.A.M. Baker, D.J. Campbell and A.E. Costley, Rev.Sci.Instr. **56**,940(1985)

10) H. Salzmann, K. Hirsch, P. Nielsen, C. Gowers, A. Gadd, M. Gadeberg, H. Murmann and C. Schrödter, Nucl.Fusion **27**,1925(1987)

11) D. Pasini, R.D. Gill, J. Holm, E. van der Goot and A. Weller, Rev.Sci.Instr. **59**,693(1988)

12) D.V. Bartlett, D.J. Campbell, A.E. Costley, N. Gottardi, C.W. Gowers, K. Hirsch, S.E. Kissel, P. Nielsen, S. Nowak, J. O'Rourke and H. Salzmann, 15th European Conference on Controlled Fusion and Plasma Heating, Dubrovnik 1988.

13) O.N. Jarvis, G. Gorini, M. Howe, J. Källne, V. Merlo, G. Sadler, and P. van Belle, 12th European Conference on Controlled Fusion and Plasma Physics, Budapest 1985.

14) T. Elevant, D. Aronson, P. van Belle, G. Grosshög, M. Hök, M. Olsson, and G. Sadler, JET-P(89)76, to appear in Nucl.Instr.Meth. (1990)

15) S. Corti, A. Boileau, G. Bracco, M. Forrest, M. von Hellermann, L. Horton, P. Larsen, C. Sack, H.P. Summers, A. Taroni and F. Tibone, 15th European Conference on Controlled Fusion and Plasma Heating, Dubrovnik 1988.

Table I

E_{phot} (keV)	L (m^2sr)	η_{4300V} (c/ph)	T	S $(\frac{c}{ph/m^2 sr})$
3.91	$2.65 \cdot 10^{-9}$	0.30	0.089	$7.2 \cdot 10^{-11}$
7.82	$4.30 \cdot 10^{-10}$	0.16	0.61	$4.2 \cdot 10^{-11}$
11.73	$8.79 \cdot 10^{-11}$	0.057	0.73	$3.7 \cdot 10^{-12}$

Table I:

The luminosity L of the germanium crystal, the relative detector efficiency η, the transmission in the rest of the diagnostic system T and the resulting absolute calibration factor $S = LT\eta$ for a detector chamber voltage of 4300 V. (Ref. 8)

Table II

Error source	Δ $T_i(0)$ (%)	$\Delta\omega_{rot}(0)$ (krad/s)	Δ f_{Ni} (%)	Δ Z_{eff} (%)
calibration				
sensitivity	—	—	±16	±16
wavelength	—	±4.0	—	—
count rate	±10	±3.0	±5.0	±13
systematic $T_e(R)$ (ECE only)				
at $T_e(0)$ = 3 keV	2.5	-0.4	-30	-20
5 keV	3.0	-0.2	-20	-10
11 keV	6.0	0.3	-5.0	-5.0
statistical $T_e(R)$ (LIDAR only)				
at $T_e(0)$ = 3 keV	5.0±2.5	-1.0±0.1	1.1±3.5	±1.0
5 keV	3.0±3.0	-0.5±0.08	0.2±2.0	±1.2
11 keV	2.5±3.0	±0.05	±1.0	7.2±4.2
systematic $n_e(R)$				
absolute level	—	—	±16	±16
profile shape	±2.0	±1.0	±15	±25
statistical $n_e(R)$				
at $T_e(0)$ = 3 keV	±0.4	±0.12	±5.5	±5.0
5 keV	±0.9	±0.14	±5.5	±3.0
11 keV	±1.4	±0.15	±4.5	±3.2

Table II:

Summary of error analysis, considering uncertainties due to instrument calibration, count rate statistics and electron temperature and density input data. The errors due to count rate statistics, calibration of the absolute sensitivity and calibration of the wavelength scale of the x-ray crystal spectrometer are discussed in III.2. The influence of electron temperature data is described in III.3.1. The systematic error refers to a change from LIDAR to ECE, the latter beeing typically 10% higher, i.e. applies to ECE only. The statistical error is based on the accuracy of the LIDAR data, which is typically 5%, i.e. applies to LIDAR only. The errors due to the electron density input data are discussed in III.3.2. The accuracy of the absolute level is estimated to be 8%. Again, the statistical error is based on the 10% accuracy of the LIDAR data.

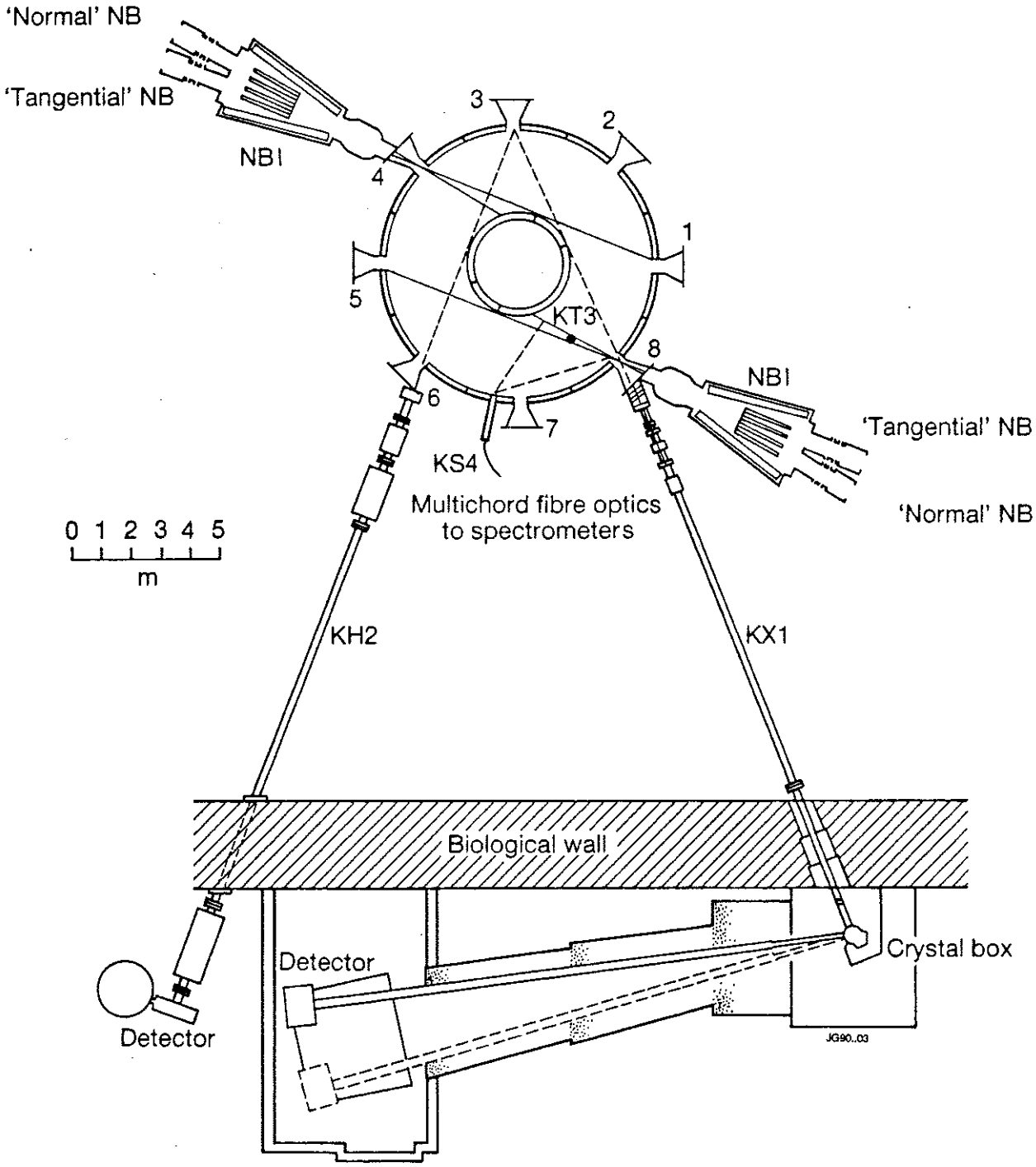

Figure 1:

Horizontal cross section of the x-ray crystal spectrometer (KX1) on the JET tokamak, showing the line-of-sight and the main geometrical dimensions. Also shown are the two neutral beam injection boxes (NBI), the pulse-height analysis system (KH2) and the line-of-sight of the various charge exchange recombination spectroscopy chords (KS4, KT3).

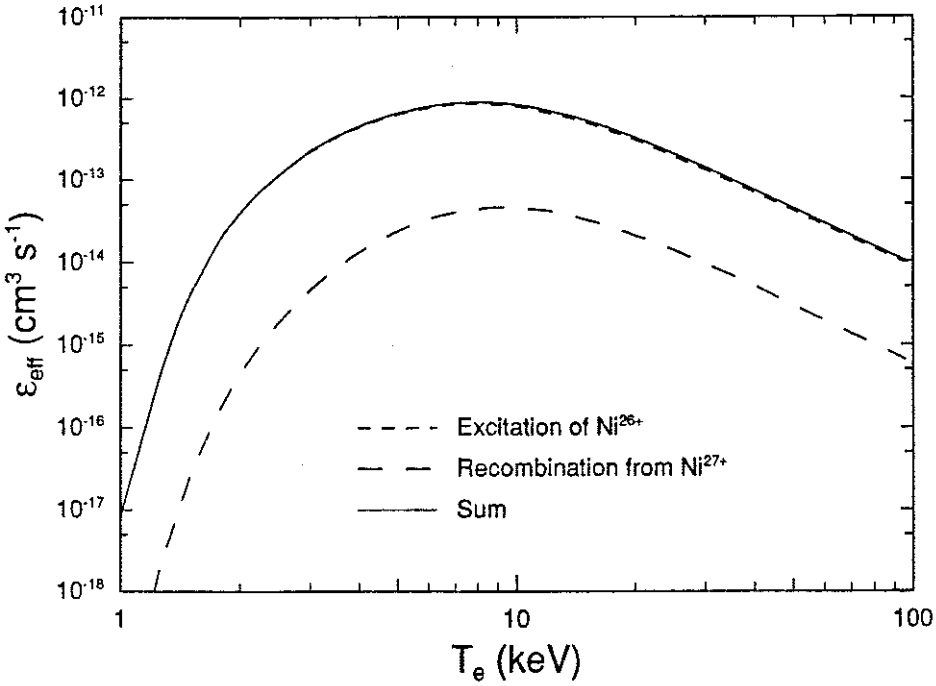

Figure 2:

Effective rate coefficient for the emission of the resonance line w of helium-like nickel as function of electron temperature. The ionisation balance, i.e. the fractional abundance of helium-like and hydrogen-like nickel, has already been taken into account. The solid line is the sum of the contributions from electron impact excitation in helium-like nickel and radiative plus dielectronic recombination from hydrogen-like nickel into the excited state of the resonance line.

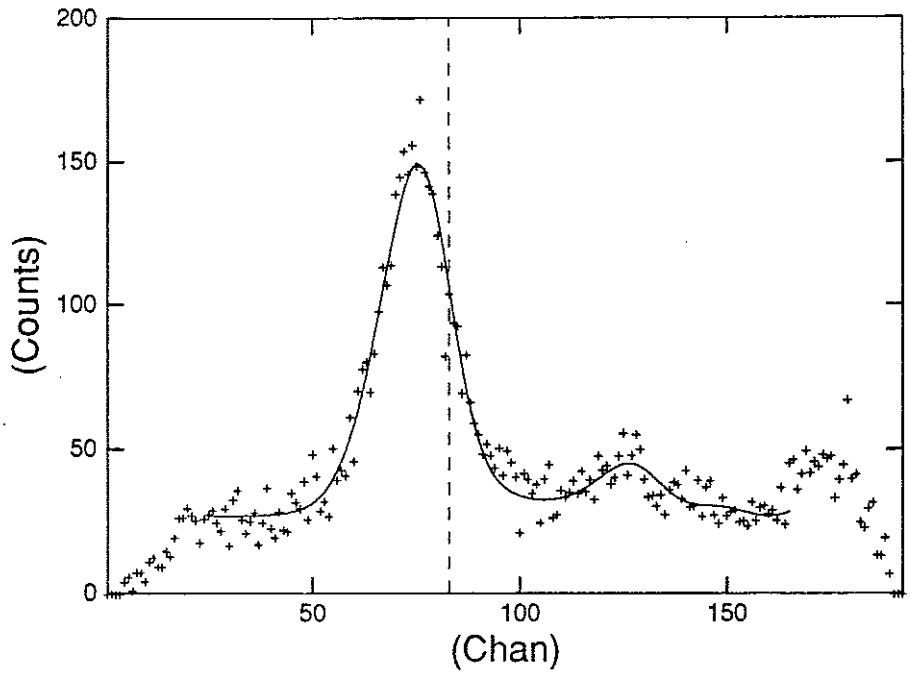

Figure 3:

Example of model fit to the spectrum of helium-like nickel and its satellite lines (JET discharge 19462, from 53.38 to 53.40 seccs). The input data and model assumptions used to obtain the fit are shown in Figs. 4, 5 and 6. The vertical dashed line marks the position of the resonance line, when the plasma is not rotating. The fraction of nickel is $4.0 \cdot 10^{-5}$ and Z_{eff} is 4.8 assuming only hydrogen as bulk plasma and the ratio of Be/C = 1/5.

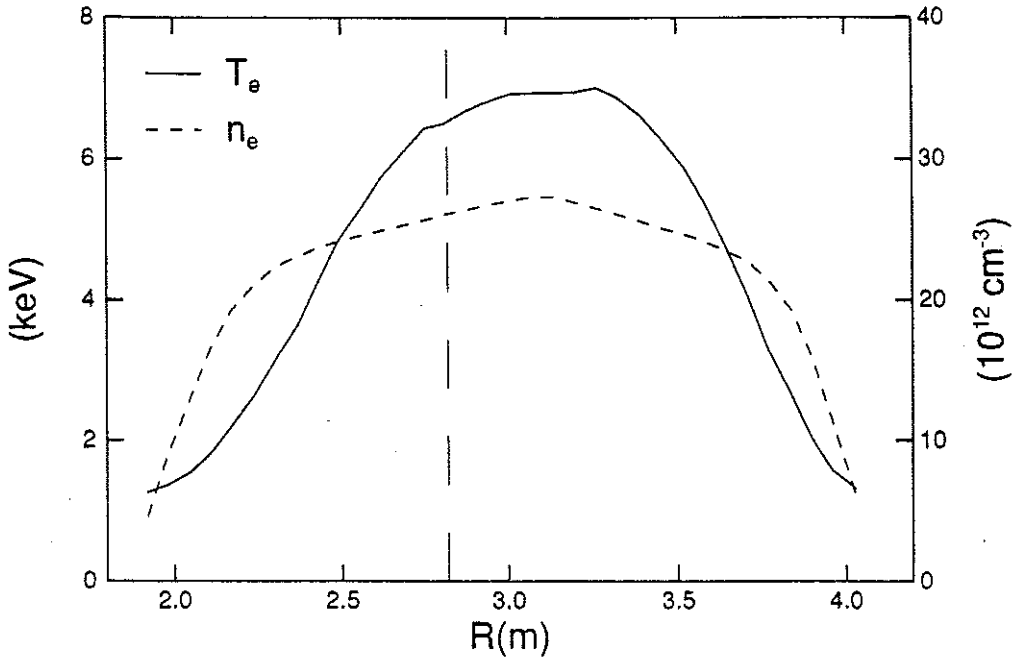

Figure 4:

Electron temperature input data from ECE and electron density input data from interferometry for the model fit in figure 3. The temperatures are measured to the right of the dashed vertical line. Electron temperature data for smaller radii are obtained, by using results from larger radii for the same flux surface label index $\Psi(R)$.

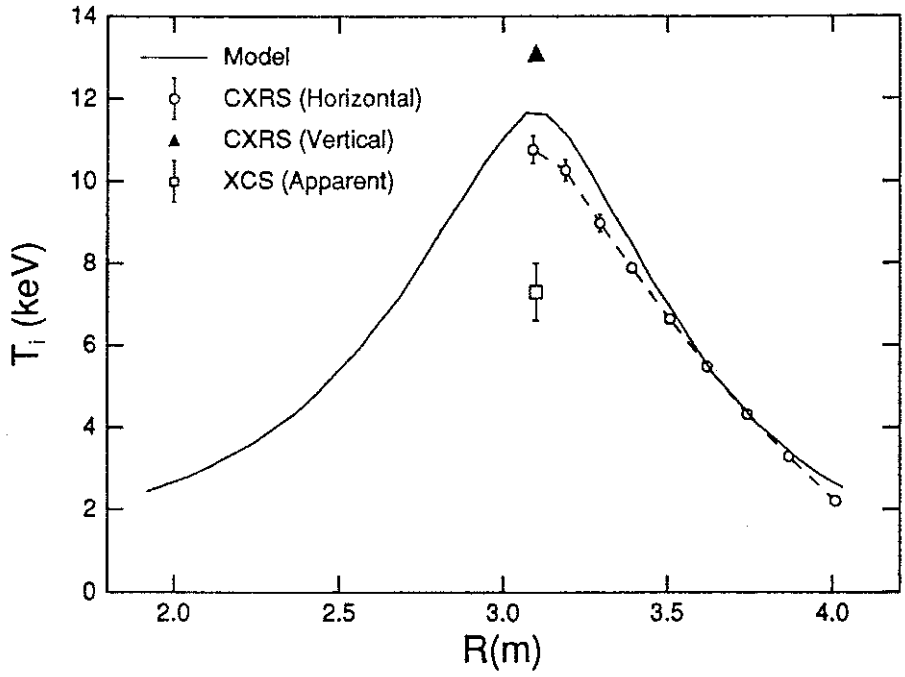

Figure 5:

Ion temperature profile from the model fit in figure 3, compared to the ion temperature profile and centre chord value from CXRS and the apparent ion temperature of the resonance line. The peaking parameter γ_T for the model profile was taken from the CXRS profile. The central value is fitted.

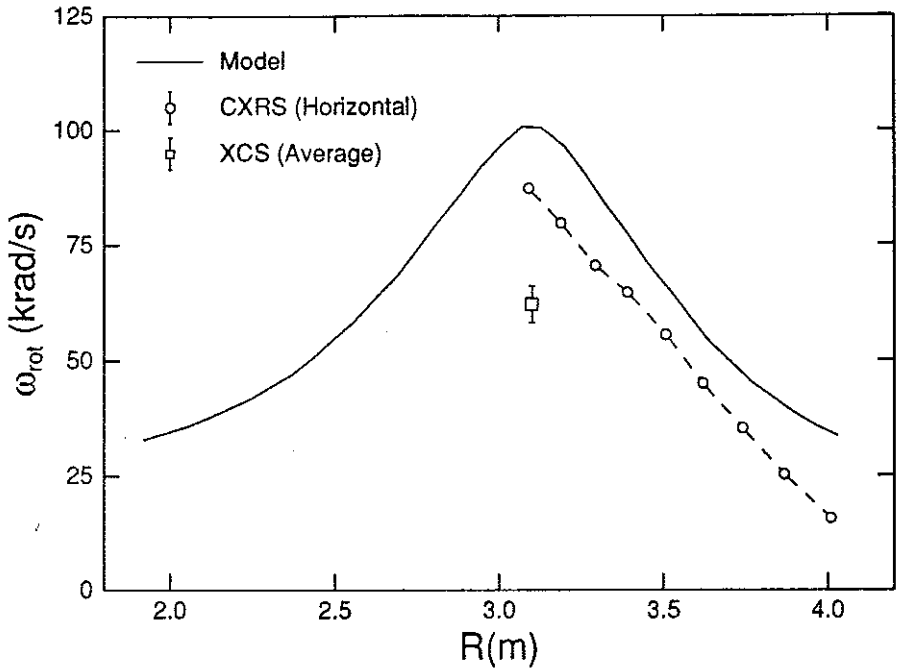

Figure 6:

Toroidal rotation profile from the model fit in figure 3, compared to the profile from CXRS and the rotation measured from the observed shift of the resonance line. The peaking parameter γ_ω for the model profile was taken from the CXRS profile. The central value is fitted.

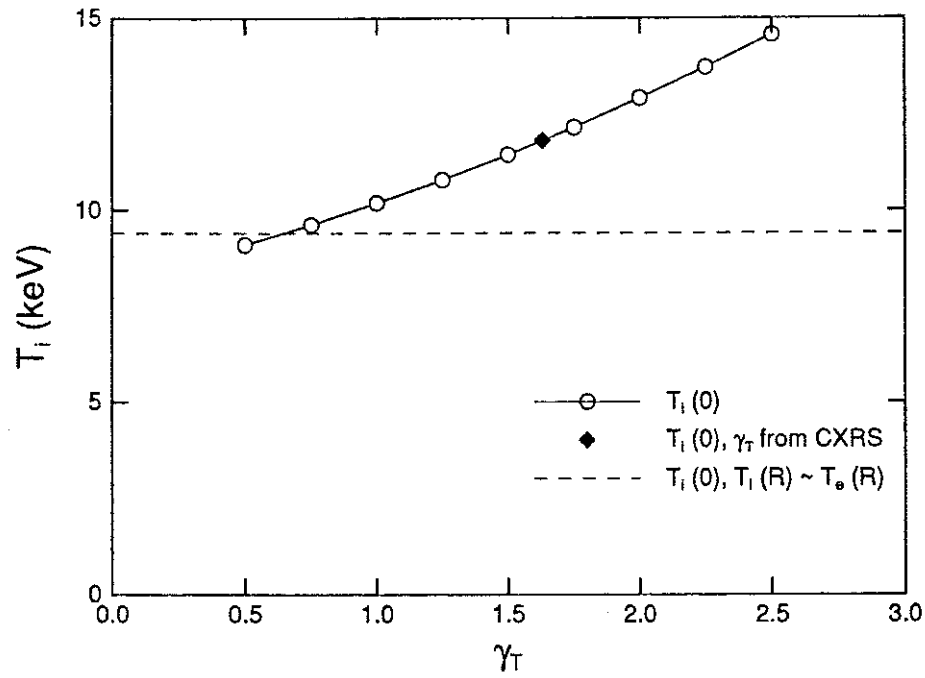

Figure 7:

Central ion temperature measured from the spectrum shown in figure 3 assuming different models for $T_i(R)$. The central ion temperature is shown as function of γ_T. Also indicated is the result using the peaking parameter from CXRS and the assumption, that the ion temperature profile is proportional to the electron temperature profile.

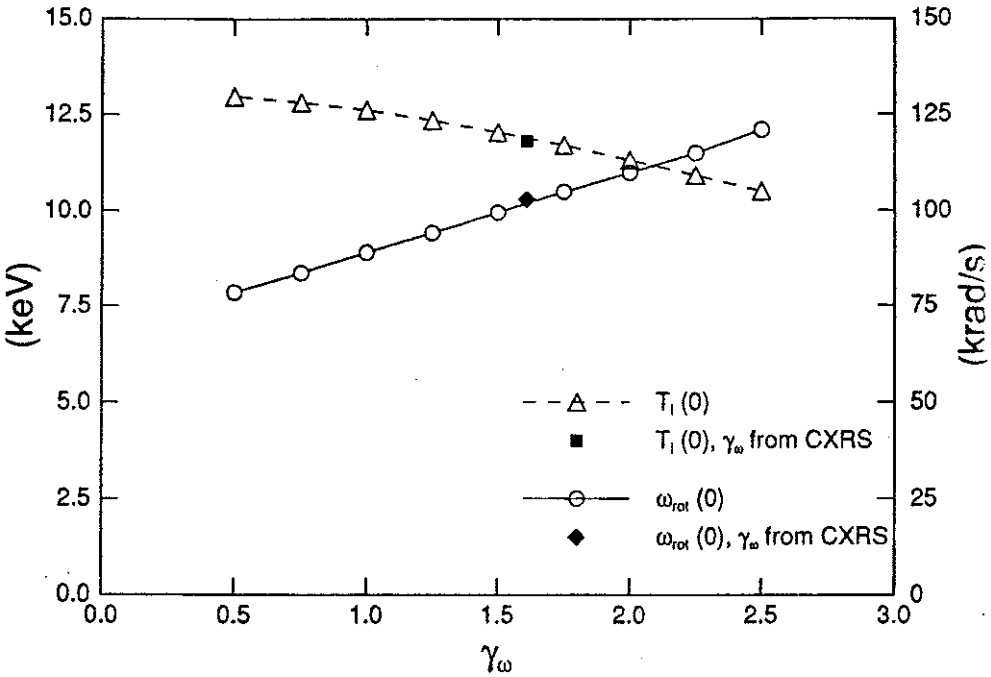

Figure 8:

Central rotation frequency and central ion temperature measured from the spectrum shown in figure 3 assuming different models for $\omega_{rot}(R)$. The central value is shown as function of γ_ω. Also indicated are the results using the peaking parameter from CXRS.

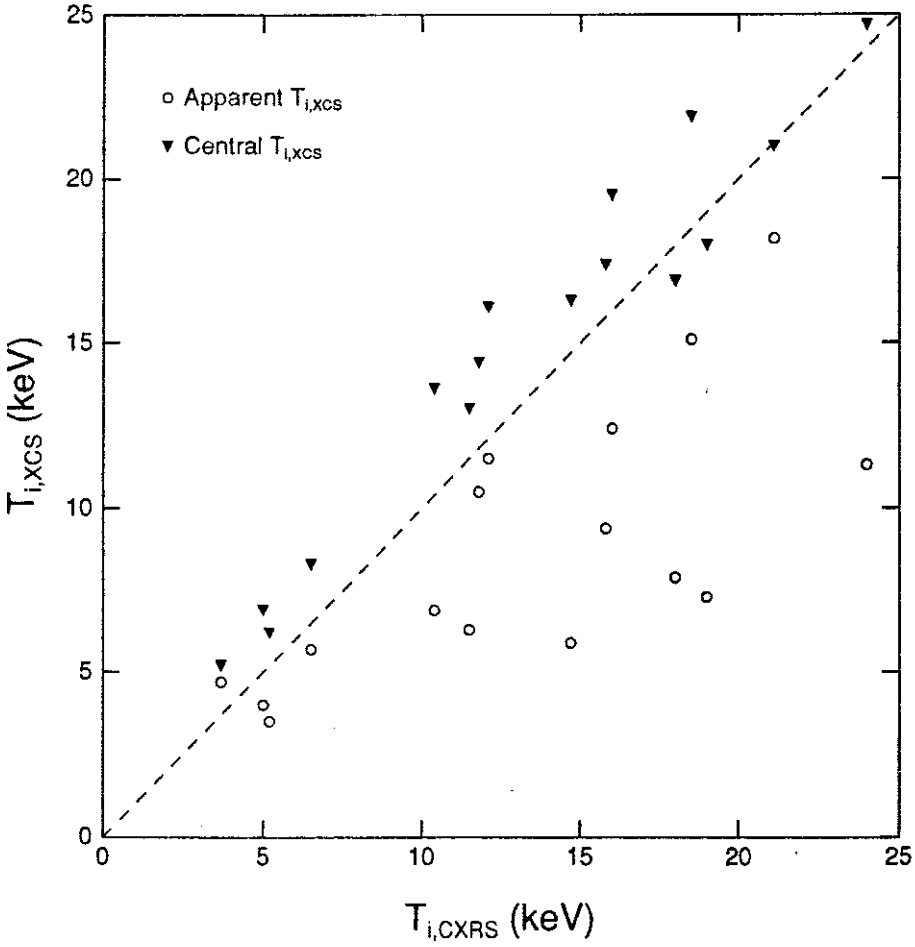

Figure 9:

Comparison of central ion temperature obtained from the model fit and apparent ion temperature with the central ion temperature from CXRS. The points are taken from several discharges at times when the beam penetration was better than 20% to guarantee good signals from CXRS.

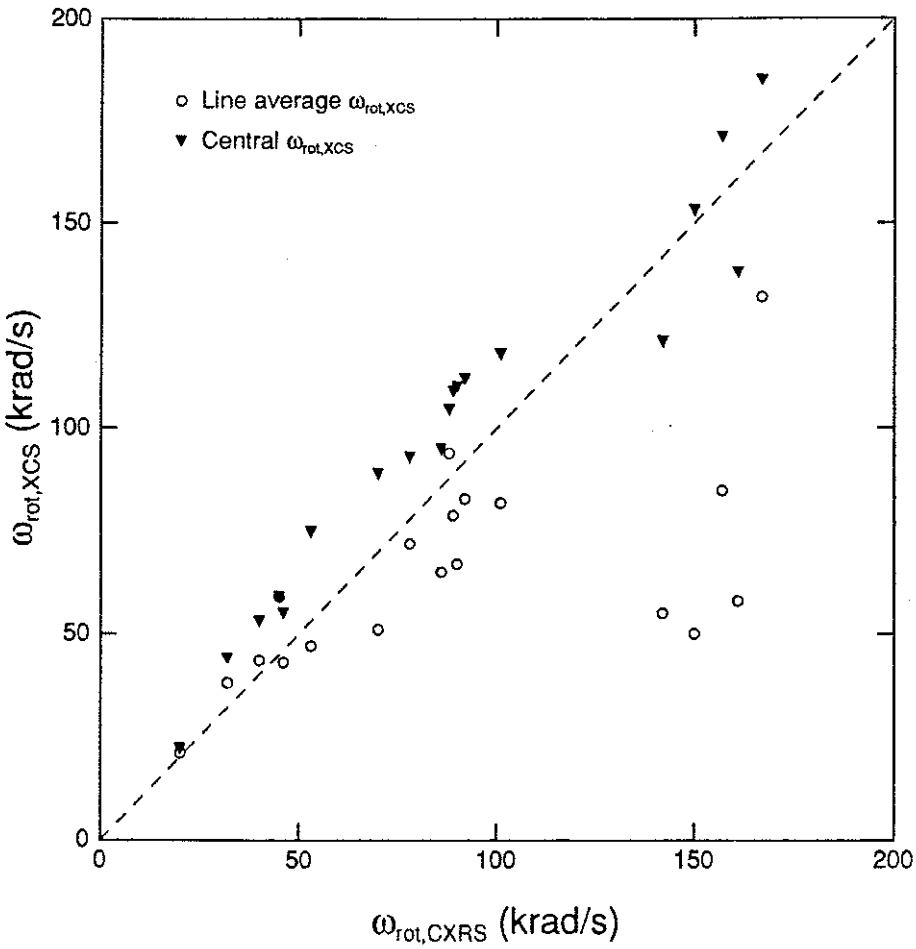

Figure 10:

Comparison of central rotation frequency from the model fit and line-of-sight average rotation frequency with the central toroidal rotation from CXRS. The points are taken from several discharges at times when the beam penetration was better than 20% to guarantee good signals from CXRS.

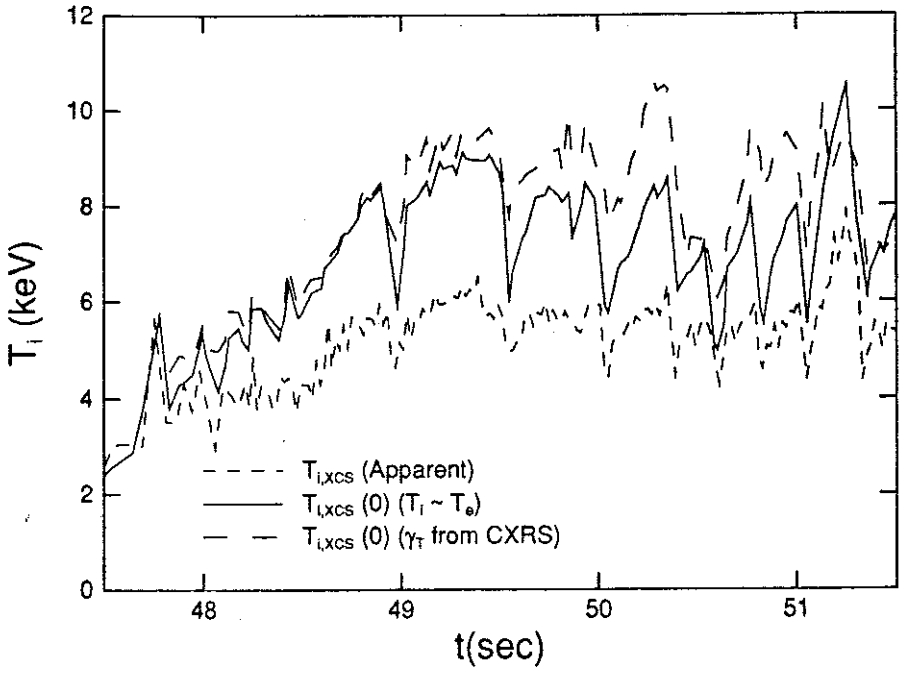

Figure 11:

Comparison of apparent ion temperature and model fit results during the NBI phase of JET discharge 19738 using different models for the ion temperature profile. The assumption, that T_i is proportional to T_e gives slightly lower values. The sawtooth crashes in $T_i(0)$ are less pronounced when peaking parameters γ_T from CXRS are used, since the CXRS detector time response is not sufficient to resolve fast changes of order 20 msec.

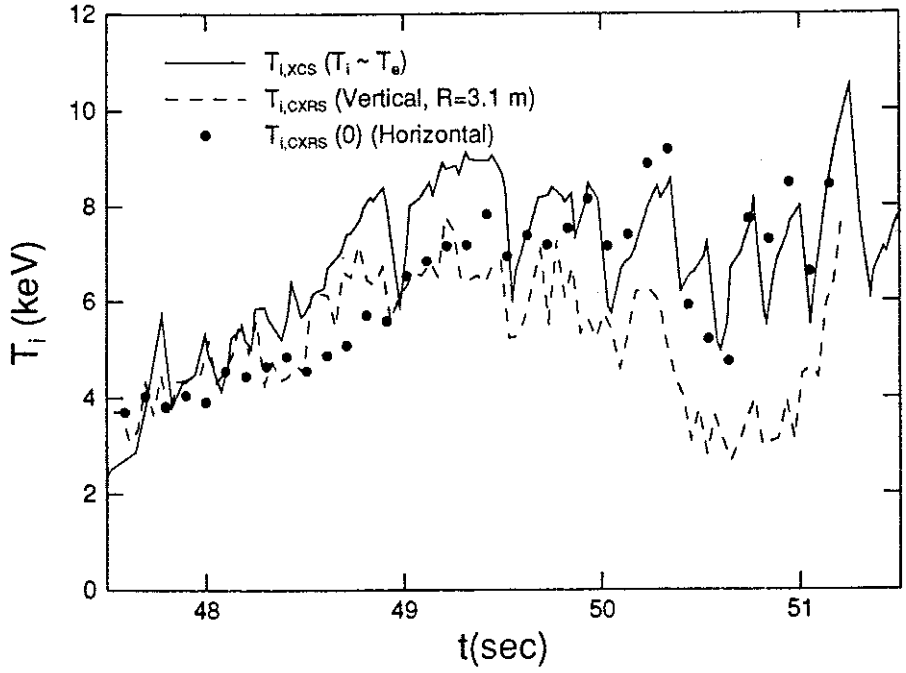

Figure 12:

Comparison of the central XCS ion temperature based on the assumption that $T_i(R)$ is proportional to $T_e(R)$ with different CXRS ion temperatures for the same discharge as in Fig. 11. The central CXRS channel has a better time resolution and response. Its line-of-sight is fixed at 3.1 m. After 50.0 secs, the magnetic axis moves and the detector does not observe the point of maximum ion temperature anymore. The results from the horizontal array have been corrected for cross section effects.

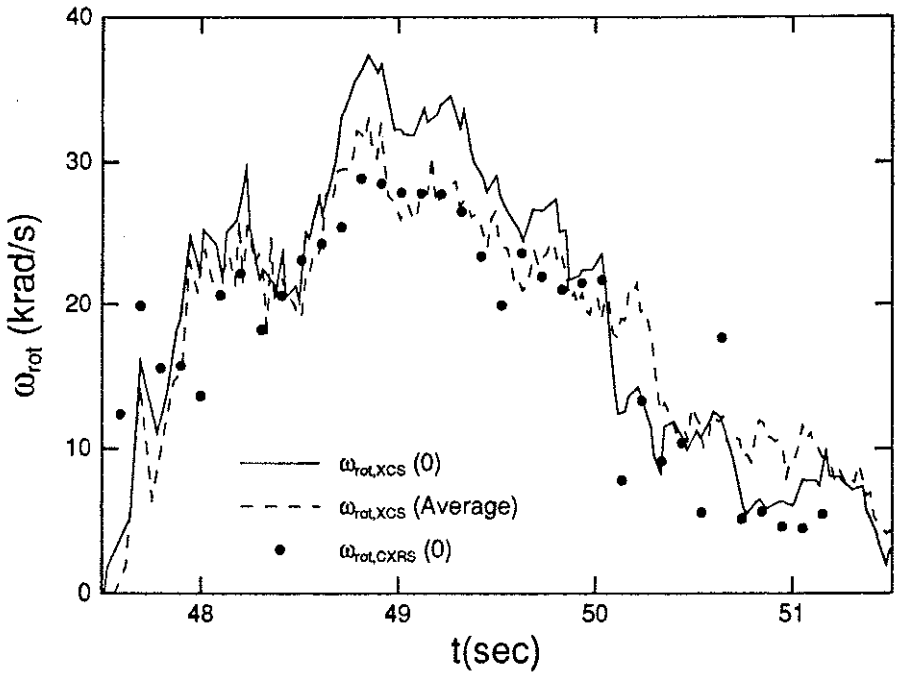

Figure 13:

Comparison of central CXRS rotation frequency, central XCS rotation frequency from the model fit using peaking parameters γ_ω from CXRS and line-of-sight average XCS rotation frequency. The results from the horizontal CXRS array have been corrected for cross section effects.

APPENDIX 1.

THE JET TEAM

JET Joint Undertaking, Abingdon, Oxon, OX14 3EA, U.K.

J.M.Adams[1], F.Alladio[4], H.Altmann, R.J.Anderson, G.Appruzzese, W.Bailey, B.Balet, D.V.Bartlett, L.R.Baylor[24], K.Behringer, A.C.Bell, P.Bertoldi, E.Bertolini, V.Bhatnagar, R.J.Bickerton, A.Boileau[3], T.Bonicelli, S.J.Booth, G.Bosia, M.Botman, D.Boyd[31], H.Brelen, H.Brinkschulte, M.Brusati, T.Budd, M.Bures, T.Businaro[4], H.Buttgereit, D.Cacaut, C.Caldwell-Nichols, D.J.Campbell, P.Card, J.Carwardine, G.Celentano, P.Chabert[27], C.D.Challis, A.Cheetham, J.Christiansen, C.Christodoulopoulos, P.Chuilon, R.Claesen, S.Clement[30], J.P.Coad, P.Colestock[6], S.Conroy[13], M.Cooke, S.Cooper, J.G.Cordey, W.Core, S.Corti, A.E.Costley, G.Cottrell, M.Cox[7], P.Cripwell[13], F.Crisanti[4], D.Cross, H.de Blank[16], J.de Haas[16], L.de Kock, E.Deksnis, G.B.Denne, G.Deschamps, G.Devillars, K.J.Dietz, J.Dobbing, S.E.Dorling, P.G.Doyle, D.F.Düchs, H.Duquenoy, A.Edwards, J.Ehrenberg[14], T.Elevant[12], W.Engelhardt, S.K.Erents[7], L.G.Eriksonn[5], M.Evrard[2], H.Falter, D.Flory, M.Forrest[7], C.Froger, K.Fullard, M.Gadeberg[11], A.Galetsas, R.Galvao[8], A.Gibson, R.D.Gill, A.Gondhalekar, C.Gordon, G.Gorini, C.Gormezano, N.A.Gottardi, C.Gowers, B.J.Green, F.S.Griph, M.Gryzinski[26], R.Haange, G.Hammett[6], W.Han[9], C.J.Hancock, P.J.Harbour, N.C.Hawkes[7], P.Haynes[7], T.Hellsten, J.L.Hemmerich, R.Hemsworth, R.F.Herzog, K.Hirsch[14], J.Hoekzema, W.A.Houlberg[24], J.How, M.Huart, A.Hubbard, T.P.Hughes[32], M.Hugon, M.Huguet, J.Jacquinot, O.N.Jarvis, T.C.Jernigan[24], E.Joffrin, E.M.Jones, L.P.D.F.Jones, T.T.C.Jones, J.Källne, A.Kaye, B.E.Keen, M.Keilhacker, G.J.Kelly, A.Khare[15], S.Knowlton, A.Konstantellos, M.Kovanen[21], P.Kupschus, P.Lallia, J.R.Last, L.Lauro-Taroni, M.Laux[33], K.Lawson[7], E.Lazzaro, M.Lennholm, X.Litaudon, P.Lomas, M.Lorentz-Gottardi[2], C.Lowry, G.Magyar, D.Maisonnier, M.Malacarne, V.Marchese, P.Massmann, L.McCarthy[28], G.McCracken[7], P.Mendonca, P.Meriguet, P.Micozzi[4], S.F.Mills, P.Millward, S.L.Milora[24], A.Moissonnier, P.L.Mondino, D.Moreau[17], P.Morgan, H.Morsi[14], G.Murphy, M.F.Nave, M.Newman, L.Nickesson, P.Nielsen, P.Noll, W.Obert, D.O'Brien, J.O'Rourke, M.G.Pacco-Düchs, M.Pain, S.Papastergiou, D.Pasini[20], M.Paume[27], N.Peacock[7], D.Pearson[13], F.Pegoraro, M.Pick, S.Pitcher[7], J.Plancoulaine, J-P.Poffé, F.Porcelli, R.Prentice, T.Raimondi, J.Ramette[17], J.M.Rax[27], C.Raymond, P-H.Rebut, J.Removille, F.Rimini, D.Robinson[7], A.Rolfe, R.T.Ross, L.Rossi, G.Rupprecht[14], R.Rushton, P.Rutter, H.C.Sack, G.Sadler, N.Salmon[13], H.Salzmann[14], A.Santagiustina, D.Schissel[25], P.H.Schild, M.Schmid, G.Schmidt[6], R.L.Shaw, A.Sibley, R.Simonini, J.Sips[16], P.Smeulders, J.Snipes, S.Sommers, L.Sonnerup, K.Sonnenberg, M.Stamp, P.Stangeby[19], D.Start, C.A.Steed, D.Stork, P.E.Stott, T.E.Stringer, D.Stubberfield, T.Sugie[18], D.Summers, H.Summers[20], J.Taboda-Duarte[22], J.Tagle[30], H.Tamnen, A.Tanga, A.Taroni, C.Tebaldi[23], A.Tesini, P.R.Thomas, E.Thompson, K.Thomsen[11], P.Trevalion, M.Tschudin, B.Tubbing, K.Uchino[29], E.Usselmann, H.van der Beken, M.von Hellermann, T.Wade, C.Walker, B.A.Wallander, M.Walravens, K.Walter, D.Ward, M.L.Watkins, J.Wesson, D.H.Wheeler, J.Wilks, U.Willen[12], D.Wilson, T.Winkel, C.Woodward, M.Wykes, I.D.Young, L.Zannelli, M.Zarnstorff[6], D.Zasche[14], J.W.Zwart.

PERMANENT ADDRESS

1. UKAEA, Harwell, Oxon. UK.
2. EUR-EB Association, LPP-ERM/KMS, B-1040 Brussels, Belgium.
3. Institute National des Récherches Scientifique, Quebec, Canada.
4. ENEA-CENTRO Di Frascati, I-00044 Frascati, Roma, Italy.
5. Chalmers University of Technology, Göteborg, Sweden.
6. Princeton Plasma Physics Laboratory, New Jersey, USA.
7. UKAEA Culham Laboratory, Abingdon, Oxon. UK.
8. Plasma Physics Laboratory, Space Research Institute, Sao José dos Campos, Brazil.
9. Institute of Mathematics, University of Oxford, UK.
10. CRPP/EPFL, 21 Avenue des Bains, CH-1007 Lausanne, Switzerland.
11. Risø National Laboratory, DK-4000 Roskilde, Denmark.
12. Swedish Energy Research Commission, S-10072 Stockholm, Sweden.
13. Imperial College of Science and Technology, University of London, UK.
14. Max Planck Institut für Plasmaphysik, D-8046 Garching bei München, FRG.
15. Institute for Plasma Research, Gandhinagar Bhat Gujat, India.
16. FOM Instituut voor Plasmafysica, 3430 Be Nieuwegein, The Netherlands.
17. Commissiariat à L'Energie Atomique, F-92260 Fontenay-aux-Roses, France.
18. JAERI, Tokai Research Establishment, Tokai-Mura, Naka-Gun, Japan.
19. Institute for Aerospace Studies, University of Toronto, Downsview, Ontario, Canada.
20. University of Strathclyde, Glasgow, G4 ONG, U.K.
21. Nuclear Engineering Laboratory, Lapeenranta University, Finland.
22. JNICT, Lisboa, Portugal.
23. Department of Mathematics, Univeristy of Bologna, Italy.
24. Oak Ridge National Laboratory, Oak Ridge, Tenn., USA.
25. G.A. Technologies, San Diego, California, USA.
26. Institute for Nuclear Studies, Swierk, Poland.
27. Commissiariat à l'Energie Atomique, Cadarache, France.
28. School of Physical Sciences, Flinders University of South Australia, South Australia SO42.
29. Kyushi University, Kasagu Fukuoka, Japan.
30. Centro de Investigaciones Energeticas Medioambientales y Techalogicas, Spain.
31. University of Maryland, College Park, Maryland, USA.
32. University of Essex, Colchester, UK.
33. Akademie de Wissenschaften, Berlin, DDR.

CR 88.49.1A